Journal of Structural Geology 32 (2010) 1476–1484

Contents lists available at ScienceDirect

Journal of Structural Geology

journal homepage: www.elsevier.com/locate/jsg

Thermal decomposition of serpentine during coseismic faulting: Nanostructures and mineral reactions

Cecilia Viti [a,*], Takehiro Hirose [b]

[a] Earth Science Department, Siena University, Via Laterina 8, 53100 Siena, Italy
[b] Kochi Institute for Core Sample Research, JAMSTEC, 200 Monobe-otsu Nankoku, Kochi 783-8502, Japan

ARTICLE INFO

Article history:
Received 29 June 2010
Received in revised form
16 September 2010
Accepted 17 September 2010
Available online 25 September 2010

Keywords:
Serpentine
Dehydration
Frictional heating
Coseismic faulting
TEM

ABSTRACT

This paper reports a detailed characterization of an antigorite-bearing serpentinite, deformed at seismic slip-rate (1.1 m/s) in a high-velocity friction apparatus. Micro/nanostructural investigation of the slip zone (200 μm thick) revealed a zonal arrangement, with a close juxtaposition of horizons with significantly different strength, respectively consisting of amorphous to poorly-crystalline phases (with bulk anhydrous composition close to starting antigorite) and of highly-crystalline assemblages of forsterite and disordered enstatite (200 nm in size and in polygonal-like nanotextures). The slip zone also hosts micro/nanometre sized Cr-magnetite grains, aligned at low angle with respect to the slipping surface and inherited from the host serpentinite.

Overall observations suggest that frictional heating at asperities on the slipping surface induced a temperature increase up to 820–1200 °C (in agreement with flash temperature theory), responsible for serpentine complete dehydration and amorphization, followed by crystallization of forsterite and enstatite (under post-deformation, static conditions). The results of this study may provide important keys for the full comprehension of the mechanical behaviour and of the possible geodynamical role of serpentinite-hosted faults through the seismic cycle.

1. Introduction

Serpentinites, predominantly formed by chrysotile + lizardite or chrysotile + antigorite associations, in pseudomorphic or interpenetrating textures, respectively (e.g., Wicks and Whittaker, 1977; Viti and Mellini, 1998; Mevel, 2003) play a key role in oceanic lithosphere dynamics, particularly in subduction and shear/fault zones.

Due to their relatively low friction coefficient (down to 0.2 for chrysotile; e.g., Reinen et al., 1991; Moore et al., 1996; Morrow et al., 2000), deformation in the oceanic lithosphere may be preferentially accommodated by serpentinitic rocks and serpentine-bearing gouges, potentially resulting in aseismic fault creep, at least at shallow conditions (Reinen et al., 1991; Moore et al., 1997; Escartin et al., 2001; Andreani et al., 2005).

However, the mechanical behaviour of serpentinites is strongly dependent on P/T conditions. In this regard, the most important process is serpentine dehydration, occurring under elevated temperature conditions. On one hand, serpentine dehydration is responsible for significant fluid release in subduction zones, with major consequences for partial melting and subduction-related magmatism (e.g., Ulmer and Trommsdorff, 1995; Ulmer, 2001). On the other hand, serpentine dehydration may result in a pore-pressure increase (possibly attaining lithostatic pressure) and ultimately in the formation of stronger anhydrous assemblages. As a consequence, serpentine dehydration is responsible for the observed temperature-dependent transition from ductile to brittle ("dehydration embrittlement"; Raleigh and Paterson, 1965), possibly leading to intermediate-depth seismicity (e.g., Peacock, 2001; Jung and Green, 2004). The mechanical effects of deformation and dehydration on serpentinites have been widely investigated both in natural context (e.g., Wicks, 1984a,b; Hoogerduijn Strating and Visser, 1994; Hermann et al., 2000; Reinen, 2000; Andreani et al., 2005; Auzende et al., 2006) and under experimental conditions (e.g., Raleigh and Paterson, 1965; Rutter and Brodie, 1988; Irifune et al., 1996; Escartin et al., 1997; Jung and Green, 2004; Hirose et al., 2006; Rutter et al., 2009; Viti and Hirose, 2009).

Serpentine dehydration can be also triggered by frictional heating during coseismic faulting, with possible consequences in fault behaviour. To help understanding the mechanical behaviour of serpentinites during the generation of earthquakes, Hirose and Bystricky (2007) performed a high-velocity friction experiment on a massive serpentinite, at conditions reproducing natural earthquake conditions, both in terms of slip velocity and displacement.

* Corresponding author. Fax: +39 577 233938.
E-mail address: vitic@unisi.it (C. Viti).

0191-8141/$ – see front matter © 2010 Elsevier Ltd. All rights reserved.
doi:10.1016/j.jsg.2010.09.009

This paper reports a detailed mineralogical and micro/nanostructural investigation of the slip zone formed during the experiment by Hirose and Bystricky (2007), focussing on serpentinite dehydration mechanism and on resulting anhydrous products. The paper aims to contribute to an increased knowledge of deformation-induced processes within serpentinite-hosted faults.

2. Experimental and starting sample

The starting sample was a natural serpentinite from Taiwan, characterized by high crystallinity and predominantly consisting of antigorite lamellae up to 80 μm in size. In order to simulate a seismogenic slip, the sample was sheared by a high-velocity friction apparatus (Hirose and Bystricky, 2007), basically consisting of a pair of cylindrical specimens of massive serpentinite pressed together with one specimen kept stationary while the other one rotated at high speed (further details in Hirose and Shimamoto, 2005). The experiment was performed at slip velocity of 1.1 m/s and normal stress of 24.5 MPa with displacements of 3.6 m under nominally-drained conditions and room temperature (run HVR694). Thus, the experimental conditions are representative of natural earthquake conditions, especially in terms of slip velocity and displacement. Humidity measurements revealed that frictional heating produced a fluid loss, soon after rapid slip initiated (run HVR694 in Hirose and Bystricky, 2007).

The sheared serpentinite was observed by Scanning Electron Microscopy (SEM) and Transmission Electron Microscopy (TEM). SEM was performed using a Philips XL30, operating at 20 kV and equipped with an EDAX-DX4 energy dispersive spectrometer (EDS), providing chemical analysis for atoms heavier than C. Counting rate was kept close to 2200–2300 counts per second over the whole energy spectrum. Analytical precision, checked by repeated analyses, was better than 0.5 wt.% for major elements (on the absolute value) and better than 20% relative for minor elements (i.e., those with contents ranging from 0.3 wt.% up to 3–5 wt.%). Back-scattered electrons (BSE) were used for image formation.

The TEM investigation was performed using a JEOL 2010 microscope, working at 200 kV, with ultra-high resolution (UHR) pole piece and point-to-point resolution of 0.19 nm. A TV-rate charge coupled device camera (Lheritier S.A. LH 74 LL) with image amplifier was used for focus and astigmatism corrections. The microscope is equipped with semi-STEM control and ultra-thin window energy dispersive spectrometer (EDS–ISIS Oxford). TEM grids were prepared from a thin section of sample HVR694, sampling a) antigorite crystals far away from the slip zone, b) the boundary between host antigorites and slip zone, and c) the slip zone. Selected grids were thinned by Ar^+ ion milling (Gatan Dual Ion Mill), from 5 to 1.5 kV and impinging angle from 20 to 12°.

3. SEM observations

Far away from the slipping zone, the starting serpentinite preserves its mineralogy and textural characteristics, showing interpenetrating undeformed antigorite lamellae, ~80 μm long, with an average SEM/EDS composition $Mg_{2.64}$ $Fe_{0.11}$ $Cr_{0.01}$ $Al_{0.11}$ $Si_{2.00}$ (atoms per formula unit, a.p.f.u., on the basis of 7 oxygens). Antigorite lamellae are associated with minor Cr-rich magnetite grains and isolated pods of brucite. Magnetite, up to millimetre in size, has highly variable Cr contents (from 1.4 to 14.8 wt.% Cr_2O_3), with ($FeO + Cr_2O_3$)/FeO ratios variable from 81 up to 96 (average value of 91).

Fig. 1a shows a representative SEM/BSE image of the sample at the slip zone, i.e., the light-grey sub-horizontal vein (double-arrowed), with ultrafine grain size. The light-grey BSE colour suggests the occurrence of a mineral association with average atomic weight higher than starting serpentinite. The slip zone, here cutting a large magnetite crystal (bright in BSE images), is characterized by the occurrence of bright elongated features aligned at low angle with respect to vein walls. The main discontinuity (broad arrow in Fig. 1a) corresponds to the slipping surface and separates the rotatory specimen (lower side in Fig. 1a) from the true slip zone. The serpentinite occurring within the rotatory side appears to be unaffected by deformation-induced transformations, as testified by its homogeneous dark-grey BSE contrast even at the boundary with the slipping surface.

The slip zone has a relatively constant thickness of 200–250 μm and often displays an asymmetric inner configuration (Fig. 1b and c), with a gradual transition from the slipping surface to the host serpentinite (stationary side). As shown in Fig. 1b, four main horizons can be distinguished. Horizon 1 consists of homogeneous and undeformed antigorite lamellae, that appear to be unaffected by possible deformation-induced processes. In horizon 2, antigorite crystals are associated with a light-grey material, occurring in thin films at grain boundaries or parallel to $(001)_{atg}$ cleavage planes (e.g., arrow in Fig. 1d) and corresponding to incipient antigorite decomposition. The boundary between horizons 2 and 3 is irregular and ill-defined (Fig. 1d and e), due to the progressive decomposition of antigorite crystals. Horizon 3 (Fig. 1e; light-grey material) is entirely formed by the antigorite decomposition products, arranged in isotropic, fine-grained textures. Based on SEM/EDS data, bulk (anhydrous) composition of horizon 3 is close to that of starting antigorite. It is worth noting that the magnetite grains occurring in horizon 3 are completely equivalent to those in the host rock, as evident in Fig. 1d showing bright crystals with unchanged size and shape. This evidence suggests that, at difference from antigorite, the Cr-rich magnetites are not affected by major deformation-induced transformations.

Horizon 4 corresponds to the true slipping zone, characterized by an ultrafine compact texture (Fig. 1f). SEM/EDS bulk data (collected on homogeneous areas, without evident magnetite grains) are equivalent to those of starting antigorite (at least, for what concerns its anhydrous composition), with average composition $Mg_{2.77}$ $Fe_{0.11}$ $Cr_{0.01}$ $Al_{0.08}$ $Si_{1.98}$ $Al_{0.02}$ (calculated on the basis of 7 oxygens for easier comparison with antigorite a.p.f.u.). Due to resolution limits, SEM investigation fails to determine the mineralogical and textural characteristics of the ultrafine-grained slipping zone, but it provides some evidence concerning the distribution of the oxide grains. As evident in both Fig. 1c and f, magnetite grains in horizon 4 have size and shape different with respect to the magnetite grains occurring within horizons 2 and 3. In particular, they are smaller in size (down to SEM resolution limits), rounded or elongated in shape, and they are aligned at low angle with respect to the slipping surface, suggesting that they were influenced by deformation. SEM/EDS data on magnetite grains within horizon 4 reveal compositions close to that of the host Cr-magnetite, with average ($FeO + Cr_2O_3$)/FeO of 91; possible minor differences in MgO and SiO_2 contents are probably related to contamination problems.

4. Mineral reactions and nanostructures

Horizons 1–4 have been investigated by high-resolution TEM, allowing accurate mineralogical and micro/nanotextural characterization. Fig. 2a shows a representative image of preserved antigorite from horizon 1 (in [010] projection), showing the recurrent features of natural undeformed and unheated antigorites, i.e., polysomatic disorder, dislocations of modulation (arrowed in Fig. 2a) and polysynthetic twinning, with typical chessboard-like texture. The inset in Fig. 2a reports the corresponding a^*c^* selected area electron diffraction (SAED) pattern, showing intense and sharp reflections; measured average superperiodicity is 40 Å (ranging

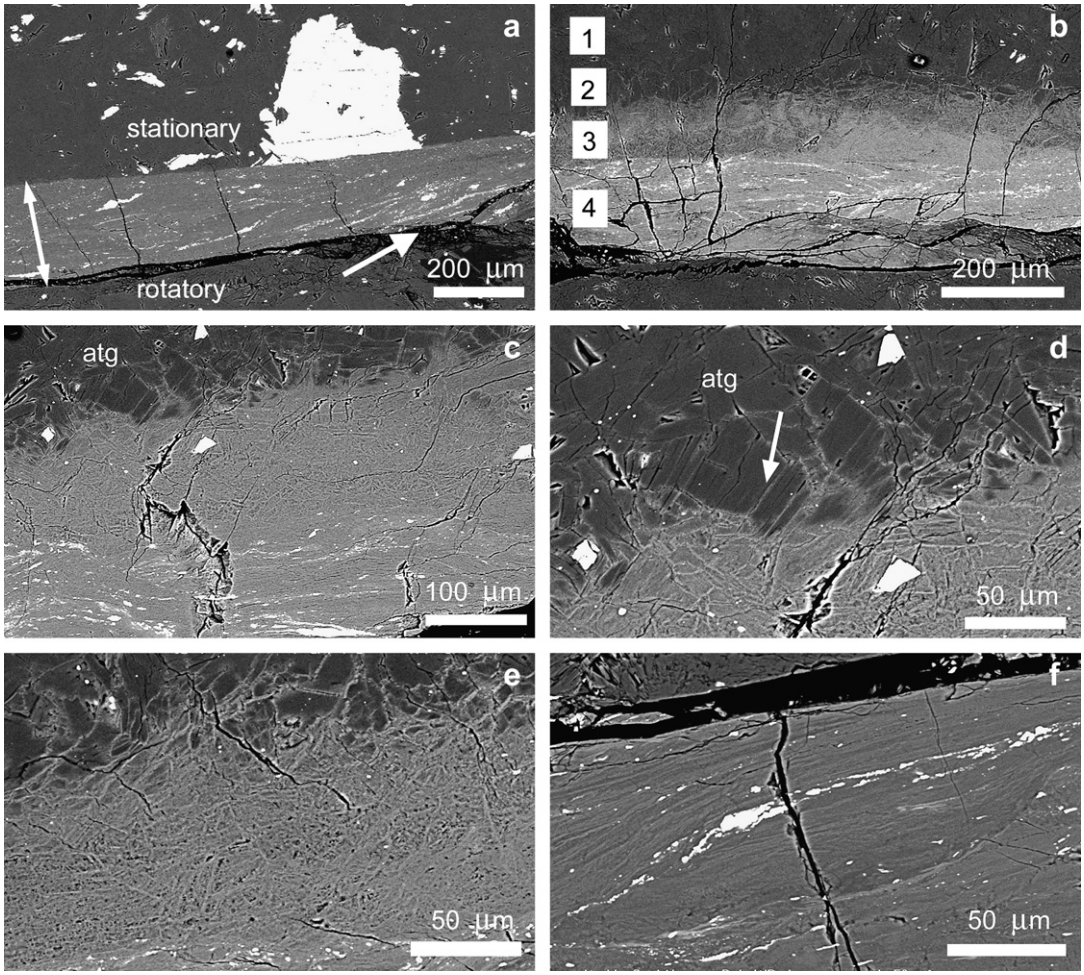

Fig. 1. (a) Slip zone (double arrowed) formed by high-velocity deformation within antigorite-bearing massive serpentinite. The broad arrow indicates the slipping surface. (b) Zonal arrangement of the slip zone with 4 main horizons consisting of un-reacted antigorite (1), partially decomposed antigorite (2), antigorite dehydration/decomposition product (3) and compact ultrafine-grained slipping zone (4). (c) Detail of the slip zone (from horizon 2 to horizon 4). (d) Irregular boundary between horizon 2 and 3; the arrow indicates early antigorite decomposition product (occurring as thin bright film parallel to $(001)_{atg}$ cleavage planes). (e) Detail of horizon 3, consisting of antigorite dehydration/decomposition product, characterized by isotropic and porous texture. (f) Detail of horizon 4, consisting of an ultrafine-grained compact material and hosting micrometer-sized magnetite grains, aligned at low angle with respect to the slipping surface. SEM/BSE images; sample HVR694.

from 38 to 44 Å). Average TEM/EDS composition is $Mg_{2.70}$ $Fe_{0.11}$ $Cr_{0.01}$ $Al_{0.07}$ $Si_{2.00}$, in good agreement with SEM/EDS results.

Moving to horizon 2, antigorite crystals appear to be partially decomposed, confirming previous hypothesis based on SEM/BSE observations. Fig. 2b displays the typical reaction boundary between crystalline antigorite (right side, dark contrast) and its decomposition product (left side), characterized by low crystallinity and high porosity. Even if irregular and undulating, the reaction front is roughly parallel to $(001)_{atg}$ planes. The decomposition product has a peculiar spongy-like texture, with fine association of thin elongated features (parallel to the original (001) planes of antigorite), rounded to elongated rods (broadly perpendicular to $(001)_{atg}$) and a large amount of pores. Based on SAED patterns, the antigorite decomposition product is predominantly amorphous, giving rise to few, weak and broad reflections. Fig. 2c shows a detail of the antigorite reaction front; the decomposition product is predominantly amorphous, except for a few crystalline portions (arrowed), with irregular 9 Å – spaced lattice fringes and probably corresponding to a transient talc-like phase (as observed in thermally-treated antigorites; e.g., Viti, 2010).

Fig. 2d shows the typical texture of horizon 3, entirely formed by antigorite decomposition products. Main differences with respect to horizon 2 are the complete disappearance of antigorite crystals, the decrease in porosity, the frequent union of nearby pores, evolving to larger elongate pores (arrows in Fig. 2d), and the occurrence of a weak anisotropy, due to the orientation of elongated pores. SAED patterns confirm the prevalence of an amorphous to poorly-crystalline material, even if the occurrence of weak, sharp reflections could suggest the occurrence of some crystalline phase (possibly, the tiny dark crystallites in Fig. 2d). Based on TEM/EDS data, the composition of the amorphous decomposition product of antigorite is highly variable, with local anomalous enrichment in silica (i.e., with tetrahedral/octahedral ratios higher than 1).

The slipping zone (horizon 4) is completely different with respect to previous horizons, being characterized by an extraordinary crystallinity, with closely associated crystals, 200–400 nm in size (Fig. 3a–d; progressively approaching the slipping surface from a to d). SAED patterns (collected in variable crystal orientations) and TEM/EDS analyses reveal that horizon 4 consists of forsterite and enstatite, with average a.p.f.u. $Mg_{1.95}$ $Fe_{0.06}$ $Si_{0.99}$ and $Mg_{1.71}$ $Fe_{0.10}$ $Al_{0.09}$ $Si_{2.05}$, on the basis of 4 and 6 oxygens, respectively. Talc was never detected. Rare relics of the poorly-crystalline antigorite decomposition product can be preserved close to horizon 3 (e.g., the ultrafine-grained lamellar features in Fig. 3a), but they disappear moving towards the slipping surface (Fig. 3b–d). Moving towards

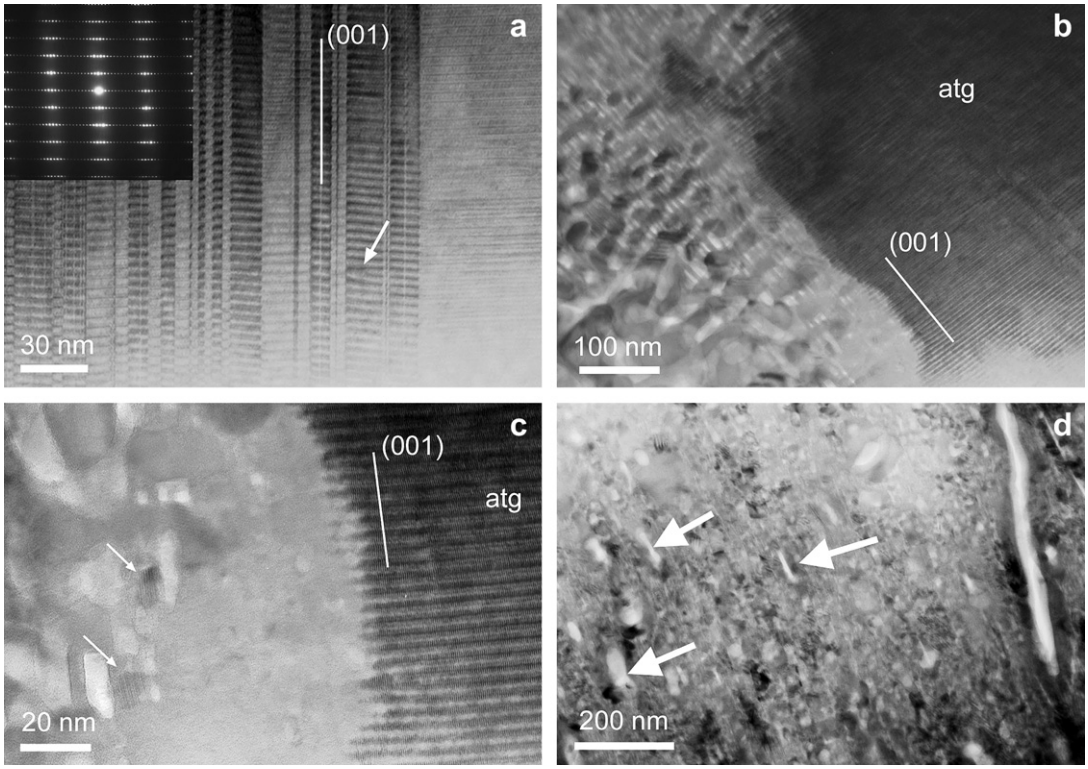

Fig. 2. (a) Representative TEM image of un-reacted antigorite from horizon 1, with (001) polysynthetic twinning and dislocations of modulation (arrow); the inset reports the corresponding a*c* SAED pattern. (b) Reaction front between preserved antigorite (dark contrast, right upper corner) and antigorite decomposition product (low contrast, left lower corner), consisting of an amorphous porous material. (c) Detail of the reaction front; arrows indicate tiny crystalline packets, with 9 Å – spaced lattice fringes. (d) Representative TEM image of the amorphous to poorly-crystalline material within horizon 3; arrows indicate elongated broad pores.

the slipping surface, horizon 4 also displays a progressive reduction in porosity and a considerable increase in grain size, evolving to "mature" compact textures with polygonal-like grain boundaries, that recall typical annealing textures (Fig. 3d).

Forsterite (slightly larger than associated enstatite) has a homogeneous TEM contrast, whereas enstatite is always characterized by a lamellar inner structure (e.g., Fig. 4a), indicative of possible structural disorder. Fig. 4b shows a detail of a forsterite crystal in [100] projection (corresponding b*c* SAED pattern in the inset), with sharp polygonal boundaries and defect-free structure. Only in rare cases, forsterite crystals display strain contrast features, suggesting limited occurrence of isolated dislocations or other structural defects (e.g., Fig. 4c and d).

At difference from forsterite, enstatite crystals are affected by intense disorder, as testified by both SAED patterns (Fig. 5a and b) and HRTEM images (Fig. 5c and d). In particular, SAED patterns have intense and continuous streaking along a*, pointing to polytypic disorder with random stacking of orthorhombic and monoclinic polytypes. HR images confirm the occurrence of randomly-stacked orthorhombic and monoclinic polytypes down to the unit-cell scale; largest ordered domains are up to 20 nm (e.g., the arrowed portion in Fig. 5c, showing a relatively ordered stacking sequence).

TEM investigation also allowed a full characterization of the oxide grains, occurring in the low-angle alignments within horizon 4. Based on SAED and TEM/EDS data, these grains still correspond to Cr-rich magnetites, with chemical composition equivalent to the Cr-rich magnetites occurring in the host serpentinite. At the TEM scale, Cr-rich magnetites within the slipping zone appear as elongated grains, up to micrometric in size, with irregular boundaries, and characterized by several strain contrast features and subgrain boundaries (e.g., Fig. 6). Overall TEM observations suggest that Cr-rich magnetite was inherited from the host serpentinite, being affected only by mechanical deformation and subsequent subgrain movements.

5. Discussion

The detailed investigation of the slip zone down to the nanoscale revealed several unexpected features that provide important information on serpentine behaviour during seismic deformation rate. Main features are summarized below.

5.1. Frictional heating and serpentine reaction

Mineralogical and micro/nanostructural observations indicate that deformation at seismic slip-rates and consequent frictional heating are responsible for serpentine decomposition. Deformation- and dehydration-induced transformations are strictly confined to the slip zone, with little heat transfer to the host serpentinite, as testified by the limited thickness of the slip zone (never exceeding 250 μm), and by the occurrence of wholly-preserved antigorite in horizon 1. Overall observations also point to the occurrence of a thermal gradient, with highest temperature at the slipping surface and progressively decreasing temperature moving towards the host serpentine.

TEM observations on horizons 2 and 3 clearly suggest that the predominant process is serpentine dehydration and amorphization. This indicates that frictional heating has at least attained the dehydration temperature of antigorite (i.e., 650–750 °C, see below). However, the possible high-temperature evolution of this material (i.e., within horizon 4, under extreme frictional heating) is not completely clear. In particular, we cannot exclude the local formation of "true" melted layer (close to the slipping surface), since the subsequent crystallization of forsterite and enstatite could have hidden any possible evidence for a previous liquid phase. The relationships between dehydration, decomposition and melting in natural pseudotachylites were previously discussed by Magloughlin and Spray (1992), according to which ferromagnesian hydrated

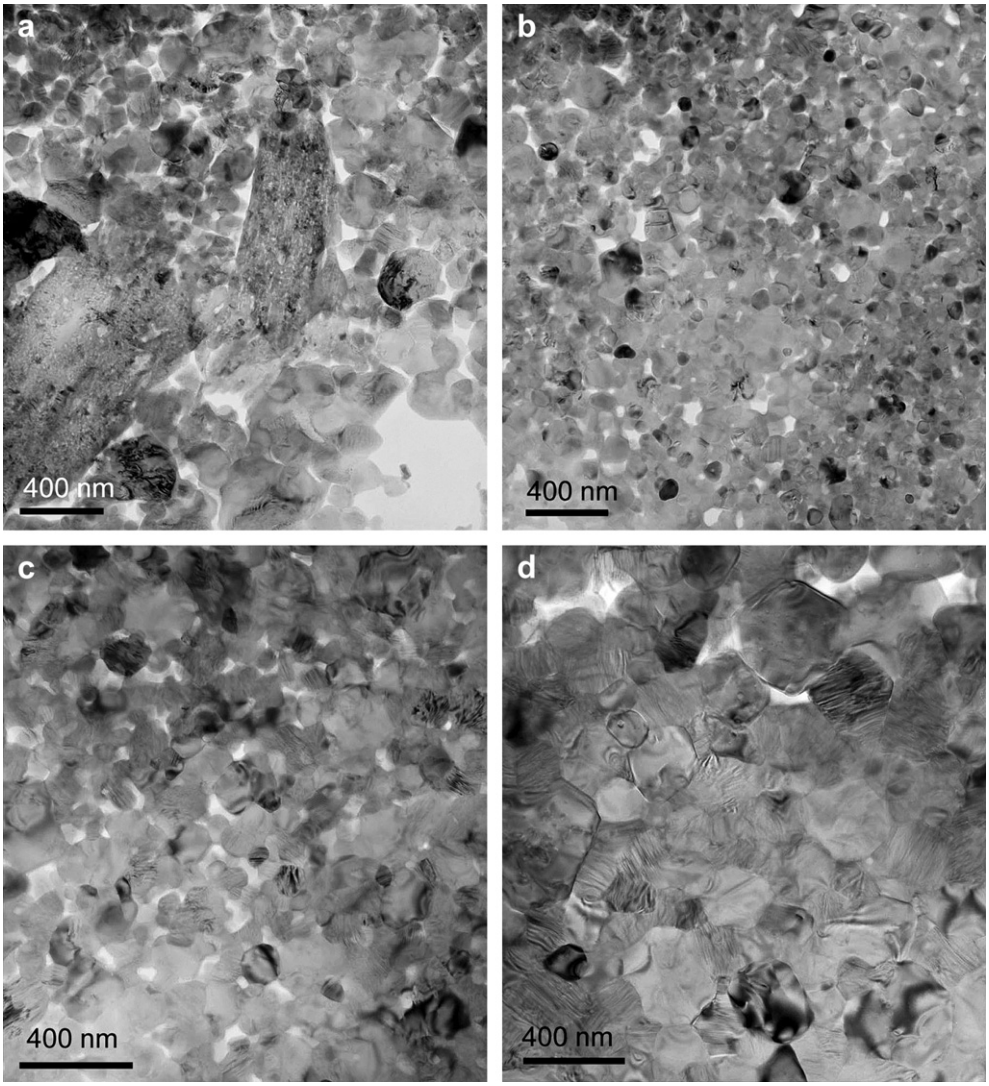

Fig. 3. TEM images of horizon 4 (slipping zone). (a) Relatively porous association of nano-crystals and lamellar poorly-crystalline material, inherited from horizon 3. (b–d) TEM images showing the progressive textural evolution of the forsterite + enstatite assemblage moving towards to slipping surface (in particular, decrease of porosity, grain size increase and development of polygonal-like nanotextures).

minerals are readily assimilated into the melt, but it is unclear to what extent mineral decomposition occurs prior to melting, during melting or after incorporation into the melt. Our observations would point to a complete decomposition prior to melting (at least in the case of serpentinitic protolites).

We also remark that, even though preserved antigorite lamellae (horizon 1) did not show clear evidences for crystal bending, subgrain boundaries and grain size reduction, those originally occurring within horizons 2 and 3 were probably affected by deformation-induced defects, resulting in enhanced reaction kinetics and in a further lowering of dehydration/decomposition temperatures (i.e., mechanochemical reactions). This hypothesis agrees with Spray (1992), reporting that at high strain rates (typical of coseismic faulting), the mechanical behaviour of minerals would be primarily controlled by their fracture toughnesses (with progressive comminution during slip), then favouring decomposition and/or melting reactions.

5.2. Static vs. dynamic crystallization

TEM observations on horizon 4 revealed the occurrence of a highly-crystalline assemblage of forsterite and enstatite. One possible issue regards the temporal sequence of crystallization and high-velocity deformation; in principle, the crystallization of the forsterite + enstatite high-temperature assemblage could have occurred during or after the slipping (i.e., under dynamic frictional heating or under static cooling, respectively), or in both conditions.

Except for the occurrence of oriented pores in horizon 3 and of low-angle alignments of Cr-magnetites grains in horizon 4, the overall slip zone appears to be dominated by isotropic textures, both at SEM and TEM scales, and it is almost unaffected by deformation micro/nanostructures. These evidences, together with the polygonal-like nanotexture observed in horizon 4, suggest that crystallization predominantly took place under static conditions. In other words, we suggest complete dehydration/amorphization of the starting serpentinite by frictional heating during high-velocity slipping, followed by structural re-arrangement with enhanced crystallization of forsterite and enstatite soon after the experiment end. Possible talc crystallization (never detected in our sample) would be hampered due to kinetic reasons, favouring fast and complete dehydration/amorphization of antigorite, followed by forsterite + enstatite crystallization under completely anhydrous conditions.

The extraordinary crystallinity of horizon 4 is quite unexpected, since it derives from a sample that have experienced an almost

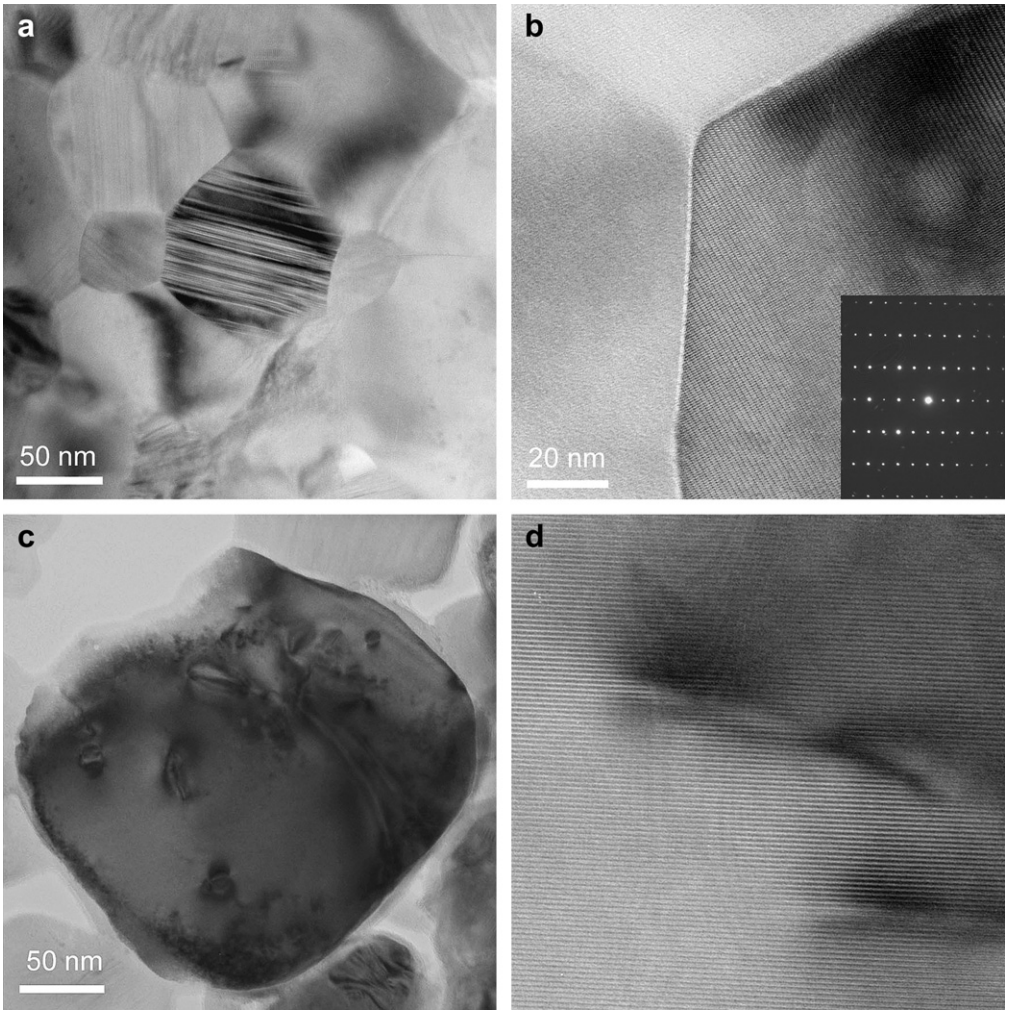

Fig. 4. (a) Close association of forsterite (homogeneous TEM contrast) and enstatite (lamellar inner nanostructure) crystals, with polygonal-like grain boundaries. (b) High-resolution detail of a forsterite crystal, showing ordered and defect-free structure; the inset reports the corresponding b*c* SAED pattern. Nearby grains correspond to forsterite in different crystallographic orientation. (c) Forsterite crystals with strain contrast features, possibly corresponding to dislocations or other structural defects; light-grey portions correspond to voids, produced by ion milling. (d) Dislocation-like defect within forsterite structure.

complete amorphization, followed by fast cooling. We suggest that crystallization and growth could be favoured by the occurrence of crystallization "seeds", corresponding to crystalline nanograins that escaped amorphization by frictional heat (i.e., the dark-contrast nanograins in Fig. 2d).

5.3. Temperature constraints

Static heating experiments on serpentine minerals (e.g., Viti, 2010; heating step of 10 °C/min and 0–1000 °C temperature range) show that antigorite dehydrates in a broad range, between 650 and 750 °C. Forsterite crystallization starts close to 750 °C (when antigorite dehydroxylation is not yet completed), whereas enstatite crystallization occurs at an extremely constant temperature of 820–830 °C (from a completely dehydrated material). The size of forsterite crystals in horizon 4, slightly larger with respect to associated enstatite, would agree with the above crystallization sequence. The occurrence of enstatite also suggests that within the slip-localized zone (i.e., within horizon 4), temperature was at least 820 °C. We remark however, that in fast heating experiment, like the one described in this paper, the estimated temperature should be considered as not-equilibrium temperature, with possible large thermal overstep.

Further temperature constraints could be provided by enstatite polytypism, in particular by the occurrence of both monoclinic and orthorhombic polytypes. In most natural occurrences, enstatite has an orthorhombic cell (space group Pbca), whereas clinoenstatite ($P2_1/c$) appears to be favoured in highly-sheared samples or in meteorites, due to possible shock effect (Raleigh et al., 1971; Smith, 1974; Iijima and Buseck, 1975; Coe and Kirby, 1975; Boland, 1977; Bozhilov et al., 1999); in addition, clinoenstatite can result from a high-T orthorhombic polytype (protoenstatite, Pbcn), stable above ~1000–1200 °C (e.g., Buseck and Iijima, 1975; Boysen et al., 1991). In our sample, clinoenstatite could be due to a Pbca (enstatite) to $P2_1/c$ transformation by high-shear strain (>10000) or to a Pbcn (protoenstatite) to $P2_1/c$ transformation by rapid quench from the high-T polytype. The observed nanotextures (pointing to static crystallization) indicate that clinoenstatite was probably formed by transformation from the high-temperature polytype, thus shifting our previous temperature estimation (i.e., ~820 °C) to ~1200 °C.

The uppermost thermal limit can be fixed on the basis of magnetite melting temperature. In fact, the occurrence of preserved magnetites within the slip zone suggests that they were not affected by decomposition or melting reactions, i.e., that the temperature locally attained by frictional heating never exceeded 1550–1590 °C (e.g., Lindsley, 1991; Deer et al., 1992).

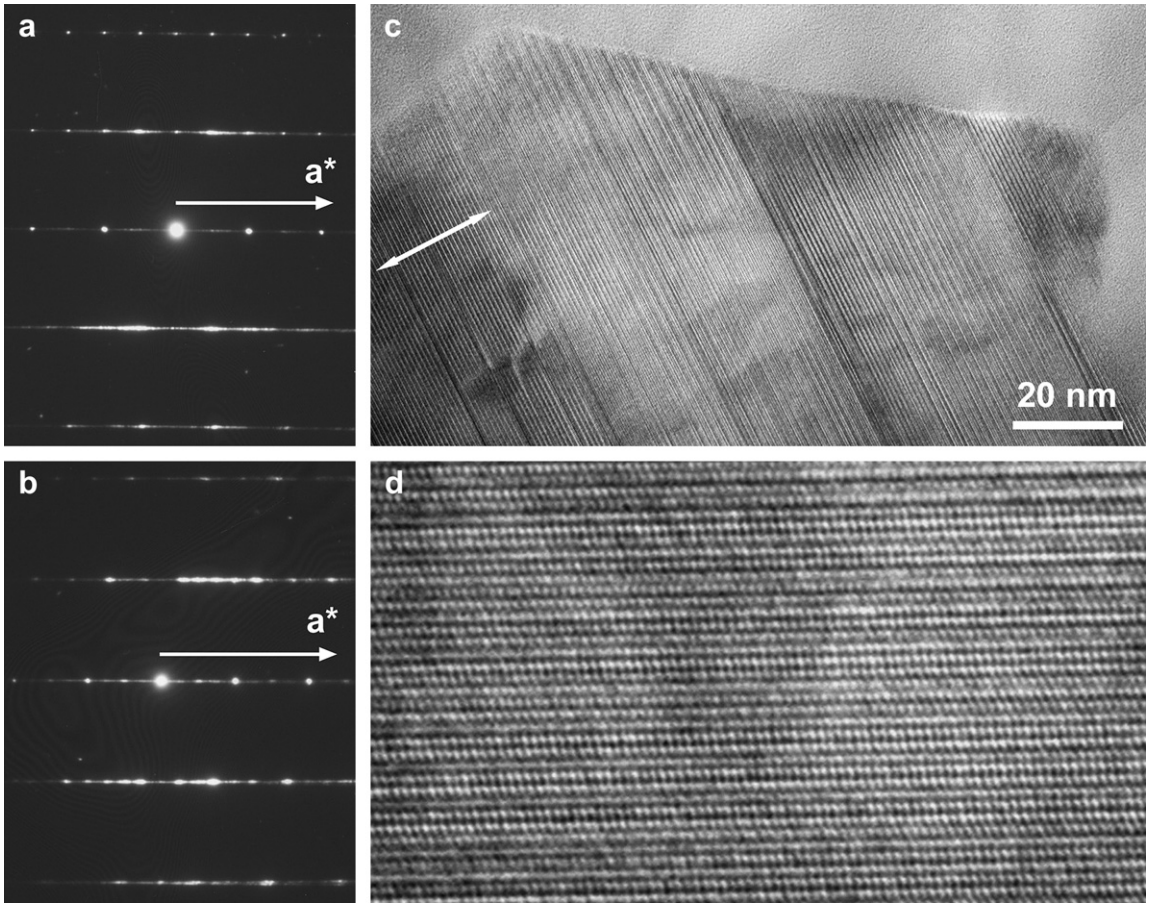

Fig. 5. (a) and (b) SAED patterns of disordered enstatite crystals, with intense a* streaking due to polytypic disorder. (c) Lamellar nanostructure in enstatite, due to randomly-stacked orthorhombic and monoclinic polytypes; relatively ordered domains can be up to 20 nm wide (double arrowed), but in most cases disorder is down to the unit-cell scale. (d) High-resolution image, showing the irregular sequence of stacking vectors in enstatite.

Overall, we conclude that the temperature within the slip zone was probably close to 1200 °C, in agreement with previous estimations (~1250 °C) based on flash temperature theory at asperity contacts and calculated by Hirose and Bystricky (2007), although their flash temperature calculation took no account of the effect of heat loss due to the endothermic reaction of serpentine dehydration and vaporization of expelled water. We also remark that the dehydration temperature of antigorite is higher than that of other phyllosilicates (e.g., clay minerals, commonly occurring along major faults), thus indicating that dehydration reactions are probably very common processes during coseismic faulting within several fault zones (e.g., Brantut et al., 2008).

5.4. Role and behaviour of Cr-rich magnetites

Serpentinitic rocks are characterized by the almost ubiquitous occurrence of spinels (usually, peridotitic Al-rich spinels or metamorphic magnetites, with variable amounts of Cr; e.g., Mellini et al., 2005 and references therein). Thus, the comprehensive knowledge of serpentinite evolution within a seismogenic fault should also take into account the behaviour and the possible role of spinels. TEM observations on Cr-magnetites within horizon 4 reveal that the temperatures induced by frictional heating were not high enough to activate magnetite decomposition/melting reactions. Instead, we suggest 1) crystal deformation with formation of subgrain boundaries; 2) fragmentation at subgrain boundaries and subsequent grain size reduction; 3) "rolling" and orientation of the fine-ultrafine subgrains with formation of the low-angle alignments (e.g., Fig. 1a and f). The resulting texture may have important implications in high magnetic susceptibility observed within slipping zones of natural seismic faults (e.g., Enomoto and Zheng, 1998; Ferré et al., 2005; Mishima et al., 2006).

5.5. Mechanical and geodynamical implications

One of the most interesting features is the close association of horizons having significantly different strength, in particular by the juxtaposition of horizons 2–3 (i.e., amorphous, partially dehydrated materials, with possible weak behaviour) and horizon 4 (i.e., compact, crystalline assemblage of relatively strong minerals such as forsterite and enstatite). This peculiar micro/nanostructure could represent a driving force to a progressive inward shift of the slipping surface (preferentially located within weak horizons). The slipping surface shift would result in a progressive thickening of the slip zone, in agreement with the observed thickness of natural pseudotachylite veins (up to centimetre thick) and with their common zonal arrangement. The overall picture suggests a cyclic process with repeated stages of cataclasis – frictional heating – dehydration/melting – cooling/crystallization. The occurrence of cyclic events was already reported by Spray (1992), for which "several cycles of mechanical breakdown – heating – melting – freezing may occur within a single slip event of several seconds duration" and "re-fracturing need not to be confined to the melted layer but may occur in the wall rock, resulting in a fault surface migration".

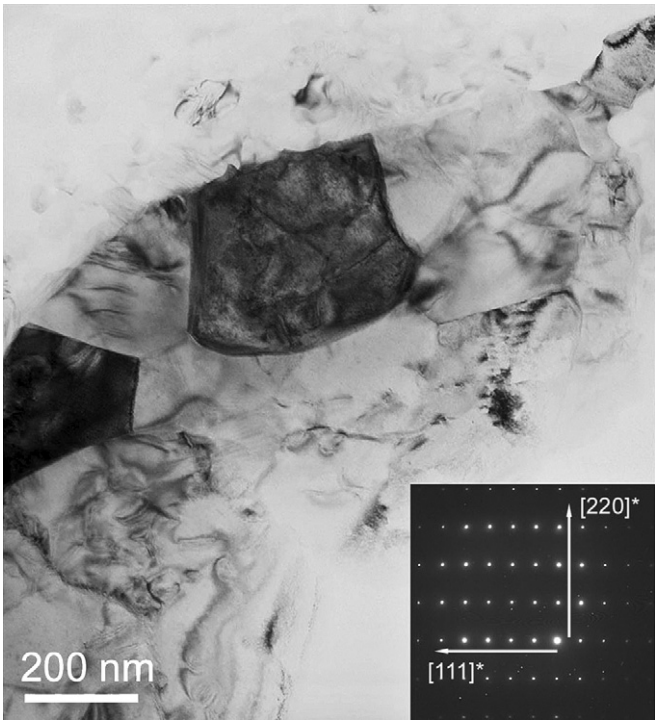

Fig. 6. Representative TEM image of large polycrystalline association of Cr-rich magnetites within horizon 4 (from low-angle alignments; e.g., Fig. 1f), showing several strain contrast features, subgrain boundaries and subgrain mis-orientations (leading to the variable TEM contrast).

The transformation of serpentine to forsterite + enstatite assemblage affects the mechanical behaviour of serpentinite-hosted faults not only during rapid sliding but also during post-sliding recovery. In particular, once rapid coseismic sliding take places in a serpentine body, the initially weak-serpentine fault (e.g., Escartin et al., 1997, 2001) could strengthen due to the formation of stronger mineral assemblage just after seismic events. Although forsterite is quite unstable at the shallow crustal depths and reacts with water to yield serpentine again (e.g., Seyfried et al., 2007), the transient formation of the relatively strong mineral assemblage in the slip-localized zone may contribute to rapid strength recovery and stress accumulation of the fault. Alternatively, at the deep crustal depths where forsterite and enstatite are mineralogically stable, transiently fine-grained products formed by a coseismic dehydration reaction may drastically release remaining stress of a main event due to grain-size sensitive plasticity processes, leading to slow earthquakes (e.g., aseismic afterslip), as observed along subduction zones.

6. Conclusions

Nanoscale investigation of slip zones (especially in the case of seismic slip-rate) may reveal unexpected features, showing complex and heterogeneous textures (more than assumed on the basis of optical microscopy or SEM observations). Seismic deformation-rate of serpentinitic rocks (and subsequent frictional heating) is responsible for important mineralogical and micro/nanotextural reactions, with complete dehydration/amorphization of serpentine, followed by crystallization of relatively strong anhydrous minerals. The overall picture (that also includes significant fluid loss, local fluid pressure increase, juxtaposition of weak and strong horizons) provides important keys for the full comprehension of serpentine behaviour in fault zones.

Acknowledgements

A.-M. Boullier and E.H. Rutter are acknowledged for their constructive comments and suggestions that greatly improved this paper. This work was funded by the Japan Society for the Promotion of Science (20740264).

References

Andreani, M., Boullier, A.M., Gratier, J.P., 2005. Development of schistosity by dissolution-crystallization in a Californian serpentinite gouge. Journal of Structural Geology 27, 2256–2267.
Auzende, A.L., Guillot, S., Devouard, B., Baronnet, A., 2006. Serpentinites in an Alpine convergent setting: effects of metamorphic grade and deformation on microstructures. European Journal of Mineralogy 18, 21–33.
Boysen, H., Frey, F., Schrader, H., Eckold, G., 1991. On the proto- to ortho-/clino enstatite phase transformation: single crystal X-ray and inelastic neutron investigation. Physics and Chemistry of Minerals 17, 629–635.
Boland, J.N., 1977. Deformation mechanisms in alpine-type ultramafic rocks from New Zealand. Tectonophysics 39, 215–230.
Bozhilov, K.N., Gree, H.W., Dobrzhinetskaya, L., 1999. Clinoenstatite in Alpe Arami peridotite: additional evidence of very high pressure. Science 284, 128–132.
Brantut, N., Schubnel, A., Rouzaud, J.N., Brunet, F., Shimamoto, T., 2008. High-velocity frictional properties of a clay-bearing fault gouge and implications for earthquake mechanics. Journal of Geophysical Research 113, B10401.
Buseck, P.R., Iijima, S., 1975. High resolution electron microscopy of enstatite II: geological application. American Mineralogist 60, 771–784.
Coe, R.S., Kirby, S.H., 1975. The orthoenstatite to clinoenstatite transformation by shearing and reversion by annealing: mechanism and potential applications. Contribution to Mineralogy and Petrology 52, 29–55.
Deer, W.A., Howie, R.A., Zussman, J., 1992. An Introduction to the Rock-forming Minerals. Longman Publisher London, 528 pp.
Enomoto, Y., Zheng, 1998. Possible evidences of earthquake lightning accompanying the 1995 Kobe earthquake inferred from the Nojima fault gouge. Geophysical Research Letters 25, 2721–2724.
Escartin, J., Hirth, G., Evans, B., 1997. Nondilatant brittle deformation of serpentinites: implications for Mohr-Coulomb theory and the strength of faults. Journal of Geophysical Research 102, 2897–2913.
Escartin, J., Hirth, G., Evans, B., 2001. Strengths of slightly serpentinized peridotites: implications for the tectonics of oceanic lithosphere. Geology 29, 1023–1026.
Ferré, E.C., Zechmeister, M.S., Geissman, J.W., Mathana Sekaran, N., Kocak, K., 2005. The origin of high magnetic remanence in fault pseudotachylites: theoretical considerations and implication for coseismic electrical currents. Tectonophysics 402, 125–139.
Hermann, J., Muntener, O., Scambelluri, M., 2000. The importance of serpentinite mylonites for subduction and exhumation of oceanic crust. Tectonophysics 327, 225–238.
Hirose, T., Shimamoto, T., 2005. Growth of molten zone as a mechanism of slip weakening of simulated faults in gabbro during frictional melting. Journal of Geophysical Research 110, B05202.
Hirose, T., Bystricky, M., Kunze, K., Stuniz, H., 2006. Semi-brittle flow during dehydration of lizardite-chrysotile serpentinite deformed in torsion: implications for the rheology of oceanic lithosphere. Earth and Planetary Science Letters 249, 484–493.
Hirose, T., Bystricky, M., 2007. Extreme dynamic weakening of faults during dehydration by coseismic shear heating. Geophysical Research Letters 34, L14311.
Hoogerduijn Strating, E.H., Visser, R.L.M., 1994. Structures in natural serpentinite gouges. Journal of Structural Geology 16, 1205–1215.
Iijima, S., Buseck, P.R., 1975. High resolution electron microscopy of enstatite I: twinning, polymorphism and polytypism. American Mineralogist 60, 758–770.
Irifune, T., Kuroda, K., Funamori, N., Uchida, T., Yagi, T., Inoue, T., Miyajima, N., 1996. Amorphization of serpentinite at high pressure and high temperature. Nature 272, 1468–1470.
Jung, H., Green, H.W., 2004. Experimental faulting of serpentinite during dehydration: implications for earthquakes, seismic low-velocity zones and anomalous hypocenter distributions in subduction zones. International Geology Review 46, 1089–1102.
Lindsley, D.H., 1991. Experimental studies of oxide minerals. In: Lindsley, D.H. (Ed.), Oxide Minerals. Reviews in Mineralogy, vol. 3. Mineralogical Society of America.
Magloughlin, J.F., Spray, J.G., 1992. Frictional melting processes and products in geological materials: introduction and discussion. Tectonophysics 204, 197–206.
Mellini, M., Rumori, C., Viti, C., 2005. Hydrothermally-reset magmatic spinels in retrograde serpentinites formation of ferritchromit rims and chlorite aureoles. Contributions to Mineralogy and Petrology 149, 266–275.
Mevel, C., 2003. Serpentinization of abyssal peridotites at mid-ocean ridges. Geoscience 335, 825–852.
Mishima, T., Hirono, H., Soh, W., Song, S.R., 2006. Thermal history estimation of the Taiwan Chelungpu fault using rock-magnetic methods. Geophysical Research Letters 33, L23311.
Moore, D.E., Lockner, D.A., Summers, R., Shengli, M., Byerlee, J.D., 1996. Strength of chrysotile-serpentinite gouge hydrothermal conditions: can it explain a weak San Andreas fault? Geology 24, 1041–1044.

Moore, D.E., Lockner, D.A., Shengli, M., Summers, R., Byerlee, J.D., 1997. Strengths of serpentinite gouges at elevated temperatures. Journal Geophysical Research 102, 14787–14801.
Morrow, C.A., Moore, D.E., Lockner, D.A., 2000. The effect of mineral bond strength and adsorbed water on fault gouge frictional strength. Geophysical Research Letters 27, 815–818.
Peacock, S.M., 2001. Are the lower planes of double seismic zones caused by serpentine dehydration in subducting oceanic mantle? Geology 29, 299–302.
Raleigh, C.B., Paterson, M.S., 1965. Experimental deformation of serpentinites and its tectonic implications. Journal of Geophysical Research 70, 3965–3985.
Raleigh, C.B., Kirby, S.H., Carter, N.L., Avé Lallemant, H.G., 1971. Slip and the clinoenstatite transformation as competing rate processes in enstatite. Journal of Geophysical Research 76, 4011–4022.
Reinen, L., 2000. Seismic and aseismic slip indicators in serpentinite gouge. Geology 28, 135–138.
Reinen, L., Weeks, J.D., Tullis, T.E., 1991. The frictional behaviour of serpentinite: implications for aseismic creep on shallow crustal faults. Geophysical Research Letters 18, 1921–1924.
Rutter, E.H., Brodie, K.H., 1988. Experimental syntectonic dehydration of serpentinite under conditions of controlled pore water pressure. Journal of Geophysical Research 93, 4907–4932.
Rutter, E.H., Llana-Funez, S., Brodie, K.H., 2009. Dehydration and deformation of intact cylinders of serpentinite. Journal of Structural Geology 31, 29–43.
Seyfried, W.E., Foustoukos, D.I., Fu, Q., 2007. Redox evolution and mass transfer during serpentinization: an experimental and theoretical study at 200 °C, 500 bar with implications for ultramafic-hosted hydrothermal systems at Mid-Ocean ridges. Geochimica et Cosmochimica Acta 71, 3872–3886.
Smith, J.R., 1974. Experimental study of the polymorphism of enstatite. American Mineralogist 59, 345–352.
Spray, J.G., 1992. A physical basis for the frictional melting of some rock-forming minerals. Tectonophysics 204, 205–221.
Ulmer, P., 2001. Partial melting in the mantle wedge: the role of H_2O in the genesis of mantle-derived arc-related magmas. Physics of the Earth and Planetary Interiors 127, 215–232.
Ulmer, P., Trommsdorff, V., 1995. Serpentine stability to mantle depths and subduction-related magmatism. Science 268, 858–861.
Viti, C., Mellini, M., 1998. Mesh textures and bastites in the Elba retrograde serpentinites. European Journal of Mineralogy 10, 1341–1359.
Viti, C., Hirose, T., 2009. Dehydration reactions and micro/nanostructures in experimentally-deformed serpentinites. Contributions to Mineralogy and Petrology 157, 327–338.
Viti, C., 2010. Serpentine minerals discrimination by thermal analysis. American Mineralogist 95, 631–638.
Wicks, F.J., Whittaker, E.J.W., 1977. Serpentine textures and serpentinization. Canadian Mineralogist 15, 459–488.
Wicks, F.J., 1984a. Deformation histories as recorded by serpentinites. I. Deformation prior to serpentinization. Canadian Mineralogist 22, 185–195.
Wicks, F.J., 1984b. Deformation histories as recorded by serpentinites. II. Deformation during and after serpentinization. Canadian Mineralogist 22, 197–203.